Journal of Heat Transfer



# Droplet evaporation of Cu-$Al_2O_3$ hybrid nanofluid over its residue and copper surfaces: towards developing a new analytical model

**Farooq Riaz Siddiqui**
Department of Mechanical and Aerospace Engineering,
The Hong Kong University of Science and Technology,
Hong Kong
frsiddiqui@connect.ust.hk

**Chi Yan Tso**
School of Energy and Environment,
City University of Hong Kong,
Hong Kong
chiytso@cityu.edu.hk

**Sau Chung Fu**
Department of Mechanical Engineering,
The University of Hong Kong,
Hong Kong
scfu@hku.hk
MASME

**Huihe Qiu**
Department of Mechanical and Aerospace Engineering,
The Hong Kong University of Science and Technology,
Hong Kong
meqiu@ust.hk

**Christopher Y. H. Chao**[1]
Department of Mechanical Engineering,
The University of Hong Kong,
Hong Kong
cyhchao@hku.hk
FASME

[1] Corresponding author Tel: +852 3917 2800, Postal Address: Department of Mechanical Engineering, The University of Hong Kong, Pokfulam Road, Hong Kong.

## Abstract

*Droplet evaporation based cooling techniques, such as the spray cooling, give high heat transfer rates by utilizing latent energy and are usually preferred in thermal applications. However, with the significant rise in heat dissipation levels for high heat flux devices, these devices cannot be thermally managed due to the limited cooling capacity of existing thermal fluids. In this paper, we report the evaporation of the Cu-$Al_2O_3$ hybrid nanofluid (HNF) droplet on a copper surface as well as its own residue surface, developed from the evaporation of the first Cu-$Al_2O_3$ HNF droplet. As the main novelty, we identify the critical residue size and investigate the residue size effect, above and below the critical residue size, on evaporation rate of the succeeding Cu-$Al_2O_3$ HNF droplet resting over a residue surface. We also develop a new analytical model to estimate the Cu-$Al_2O_3$ HNF droplet evaporation rate and compare our results with other existing models. The results show that the Cu-$Al_2O_3$ HNF droplet gives 17% higher evaporation rate than a water droplet on a copper surface. Also, the evaporation rate of the Cu-$Al_2O_3$ HNF droplet on a residue surface sharply increases by 106% with increasing residue size up to the critical residue size. However, further increasing the residue size above its critical value has a negligible effect on the droplet evaporation rate. Moreover, the evaporation rate of the Cu-$Al_2O_3$ HNF droplet on its residue surface is enhanced up to 104% when compared to a copper surface.*


*Keywords*: Evaporation; hybrid nanofluid droplet; critical residue size; wetting; pinning; roughness.

## 1. Introduction

Droplet evaporation is a latent heat transfer process that is used in many engineering applications such as fuel injection, spray cooling, inkjet printing and hotspot cooling in electronic devices. It offers high heat rejection rates as it undergoes a phase change process and is preferred over single-phase heat transfer processes in thermal applications. However, with advancement in technology, such as high computing performance, 3-D electronic packaging and chip

63 miniaturization, heat dissipation levels go beyond the thermal limit of existing heat transfer fluids
64 (i.e., > $10^6$ W/m$^2$, which is the critical heat flux (thermal limit) of water in pool boiling [1,2]). Heat
65 dissipation density in future electronic devices is anticipated to exceed $10^7$ W/m$^2$ [3]. Therefore,
66 fluids with advanced thermal properties, such as nanofluids, can be suitable alternatives for
67 effective cooling of high heat flux devices.
68
69 Nanofluid is a colloidal suspension comprising nano-sized particles (<100 nm) with advanced
70 thermal properties. It is the high thermal conductivity of these dispersed (typically metal-oxide,
71 metal or non-metal) nanoparticles that improves the thermal properties of the base fluid depending
72 on its concentration, as reported by the research community [4–6]. There are several factors that
73 affect the nanofluid thermal conductivity such as the temperature, base fluid and particle size,
74 shape and concentration [7]. The high thermal conductivity in nanofluids leads to high heat transfer
75 coefficient (as heat transfer coefficient depends on fluid thermal properties [1]) that results in
76 higher evaporation rate in nanofluid droplets than base fluid droplets on heated surfaces [8,9].
77 Although nanofluids exhibit considerably higher critical heat flux (thermal limit) than
78 conventional fluids (such as water) in phase change processes [10], the underlying physics for
79 critical heat flux enhancement in nanofluids is still unclear to the research community. However,
80 the enhanced surface wettability, roughness and wicking effect due to the nanoparticle deposition
81 on a heated surface during the phase change process are considered as possible reasons for high
82 critical heat flux in nanofluids [11,12]. Despite thermal benefits of nanofluids over conventional
83 heat transfer fluids, the former do not exhibit overall hydrothermal characteristics (high dispersion
84 stability and enhanced thermal conductivity). For example, metal based (such as Ag, Cu, Zn etc.)
85 nanofluids exhibit enhanced thermal conductivity; however, their dispersion stability is low and

they show rapid sedimentation. Conversely, metal-oxide based (such as MgO, $Al_2O_3$, ZnO etc.) nanofluids have relatively low thermal conductivity but they are more stable than metal based nanofluids. Therefore, single particle based nanofluids are not viable options for practical applications as these fluids do not exhibit overall hydro-thermal properties [13–15].

In recent years, researchers proposed the next generation of nanofluid and named it 'hybrid nanofluid'. Hybrid nanofluid (HNF) is a suspension of two different types of nanoparticles in a base fluid with improved stability and enhanced thermal properties, making it more favourable for heat transfer applications. Siddiqui et al. [16] studied the effect of hybrid nanoparticle mixing ratio on stability and thermal conductivity of the Cu-$Al_2O_3$ HNF. They concluded that 0.5:0.5 mixing ratio gives better stability and improved thermal conductivity as compared to other mixing ratios. Besides improved hydro-thermal properties, hybrid nanofluids also possess synergistic thermal characteristics, exhibiting higher thermal conductivity than single particle nanofluids [17–20]. Researchers reported thermal conductivity enhancement between 7% and 32% for Ag-MgO, $SiO_2$-MWCNT, Ag-GNP, MgO-SWCNT and $Al_2O_3$-CNT hybrid nanofluids at a low particle volume concentration of 0.05-2% [21–25]. Such a high thermal conductivity and improved stability of hybrid nanofluids make them promising candidates for high heat flux applications.

Although droplet evaporation based on single particle nanofluid has been comprehensively studied [26–28], hybrid nanofluid based droplet evaporation has received little or no attention from researchers. The hybrid nanofluid based droplet evaporation may have high heat flux removal rates than water or single particle nanofluid based droplet evaporation. Since the evaporative heat flux removal rate is the product of the evaporative mass flux and the latent heat of vaporization [1], the

advanced thermal properties of hybrid nanofluid droplets may result in their enhanced evaporative mass flux and consequently higher heat flux removal rates than water or single particle nanofluids. Besides several factors, such as the humidity, temperature, contact angle, contact radius, interfacial tensions and substrate roughness, the concentration and type of suspended nanoparticles also affect the droplet evaporation rate [29–32]. The suspended nanoparticles move towards the three-phase contact line during evaporation, where they deposit and pin the droplet to a substrate [33–35]. The deposited nanoparticles form a nanostructured residue at the end of droplet evaporation. Despite extensive research on various residue patterns obtained from droplet evaporation [27,36–38], the effect of residue remaining from the first evaporating droplet, on the evaporation rate of succeeding droplets is not studied to the best knowledge of the authors. The residue effect on the succeeding droplet evaporation rate may be extremely important to consider in dropwise or spray-cooling applications and may influence their overall heat transfer effectiveness.

The main aim of this proposed research is to study the residue effect on evaporation rate of the succeeding Cu-$Al_2O_3$ HNF droplet resting over the residue surface, developed from the evaporation of the first Cu-$Al_2O_3$ HNF droplet. We recently studied the evaporation of silver-graphene (Ag-GNP) hybrid nanofluid droplets on their residue surfaces [39], where our main focus was to examine the effect of the hybrid nanoparticle mixing ratio on droplet evaporation rate. However, in this study, our key objective is to investigate the effect of the critical residue size on evaporation rate of the following Cu-$Al_2O_3$ HNF droplet. In our previous study, the reason for using the Ag-GNP hybrid nanofluid in droplet evaporation investigation was its synergistic thermal conductivity (higher than both Ag and GNP single particle nanofluids) [39], while our motivation to use the Cu-$Al_2O_3$ hybrid nanofluid in this study is its unique overall hydrothermal

properties (enhanced thermal conductivity and high stability). Furthermore, in current research, we developed an improved analytical model without any fitting parameters compared to a semi-empirical model developed in our previous research [39]. Our main novelty in this research is the identification of the critical residue size and its effect on evaporation rate of the succeeding Cu-$Al_2O_3$ HNF droplet sitting on a residue surface. In this research, we showed that as evaporation ended, the Cu-$Al_2O_3$ HNF droplet formed a partially wetted residue surface. The succeeding Cu-$Al_2O_3$ HNF droplet, sitting on a residue from the first droplet, spread to its boundary for all residue sizes up to the critical residue size. In this way, a range of droplet evaporation rates was obtained for succeeding droplets sitting on a residue surface by varying the residue size up to the critical residue size. On the other hand, as the residue size exceeded its critical value, the succeeding droplet remained unbounded (did not reach the residue boundary) on a residue surface, giving similar evaporation rates for all residue sizes above the critical residue size. Thus, the critical residue size is an important parameter affecting the evaporation rate of the succeeding droplet sitting over the residue surface. This residue size based droplet evaporation can be important in spray cooling applications, where residues of different sizes, formed by poly-disperse or coalesced and non-coalesced spray droplets, may have different effect on evaporation rate of succeeding droplets. Moreover, as copper is most commonly used in heat exchangers and other heat transfer applications, besides the residue surface, we also studied the evaporation rate of the Cu-$Al_2O_3$ HNF droplet on a copper surface and compared results with a water droplet on a copper surface.

In this research, as discussed, we developed a new analytical model that can estimate the Cu-$Al_2O_3$ hybrid nanofluid droplet evaporation rate on both copper and residue surfaces with higher accuracy as compared to our recently developed semi-empirical model [39]. Although both models

are based on the Fick's law of mass diffusion, the semi-empirical model [39] involved a correlated vapour concentration gradient term ($dx_v/dh$) that was directly obtained from the experimental data. Conversely, in this study, the Fick's law of mass diffusion is analytically solved thus making the current model independent of any fitting parameters. Moreover, our proposed analytical model in this research is based on the droplet radius of curvature and considers evaporation in all directions (vertical and radial) above the droplet-air interface. However, our semi-empirical model [39] was based on the droplet height and only considered evaporation in a vertical direction (along the height) above the droplet-air interface. Due to this reason, the proposed analytical model in this study offers better estimation for the considered Cu-$Al_2O_3$ hybrid nanofluid droplet evaporation rate than our semi-empirical model [39], as further discussed in results and discussion section. Although various theoretical models were developed in the past to predict the droplet evaporation rate [40–43], most of them are approximate solutions based on the droplet contact angle. Another limitation is that some of these models do not cover a wide contact angle range and are only applicable for droplet contact angles below 90°. Unlike other models, our proposed analytical model can also be applied for droplets with high contact angles (> 90°). However, our model can only be used for pinned droplets with constant contact radius, as is the case of considered Cu-$Al_2O_3$ hybrid nanofluid droplets in this research. Therefore, our model cannot estimate the evaporation rate of water droplets, as these droplets de-pin on a smooth copper surface during evaporation. Furthermore, we studied the effects of residue surface free energy and its roughness on wetting and evaporation rate of the Cu-$Al_2O_3$ HNF droplet sitting over a residue surface. Following is a summary of key objectives of our research:

- To study the evaporation rate and wetting behaviour of the Cu-$Al_2O_3$ HNF droplet and compare it with a water droplet over a copper surface.

- To identify the critical residue size and investigate the residue size effect, above and below the critical residue size, on wetting and evaporation rate of succeeding Cu-$Al_2O_3$ HNF droplets.
- To develop a new analytical model to estimate the Cu-$Al_2O_3$ HNF droplet evaporation rate.

## 2. Experimental techniques

### *2.1. Hybrid nanofluid preparation*

A two-step approach was used to prepare the Cu-$Al_2O_3$ hybrid nanofluid (HNF) in which copper (25 nm particle size) and $Al_2O_3$ (13 nm particle size) nanoparticles were dispersed in de-ionized water and ultra-sonicated for 0.5 hours. This ultra-sonication time gives the highest dispersion stability when compared to other ultra-sonication times, as reported in our previous study [44]. Due to the high thermal conductivity and improved dispersion stability of Cu and $Al_2O_3$ nanoparticles respectively, we selected these particles for hybrid nanofluid synthesis in our study. Furthermore, we fixed the particle volume fraction at 0.1%, as the effect of particle concentration on droplet evaporation rate is not the objective of this study. Based on our recent study [16], we used a mixing ratio of 0.5 (Cu):0.5 ($Al_2O_3$) by volume for the Cu-$Al_2O_3$ HNF in this study, as this mixing ratio gives better overall hydrothermal properties, compared to other mixing ratios. The procedure to prepare Cu-$Al_2O_3$ HNF is discussed in detail by Siddiqui et al. [16].

### *2.2. Droplet evaporation rate and contact angle measurements*

The evaporation, contact angle and contact radius of 3 µl volume of the Cu-$Al_2O_3$ hybrid nanofluid and water droplets were analysed using an optical tensiometer (Theta, Biolin Scientific, Finland) at relative humidity of $\varphi$ = 0.3 and room temperature (22 °C), without substrate heating.

Prior to droplet evaporation experiments, residues with 9 different sizes were developed on a smooth copper surface using the Cu-$Al_2O_3$ hybrid nanofluid droplet volume of 1.5 µl, 3 µl, 6 µl, 9 µl, 12 µl, 15 µl, 18 µl, 30 µl and 60 µl. The optical tensiometer was calibrated using a tungsten carbide ball with an error of 2.86% between the calibrated volume and the true volume of the tungsten carbide ball. A 3µl volume of the Cu-$Al_2O_3$ hybrid nanofluid droplet was gently placed over the substrate (copper or residue) surface by the tensiometer dispenser. Due to slow evaporation dynamics at room temperature, the droplet images, along with the droplet volume, contact diameter and contact angle, were recorded at 1.4 frames per second until the droplet evaporation process ended. In this way, the droplet evaporation rate was obtained as the ratio of the difference of initial and final droplet volumes to total evaporation time. For the Cu-$Al_2O_3$ HNF droplet sitting on a residue surface, 9 different droplet volume ratios were used as $V_{fd}/V_{sd}$ = 0.5, 1, 2, 3, 4, 5, 6, 10 and 20, where we increased the first droplet volume ($V_{fd}$) to develop a residue, while we fixed the second droplet volume ($V_{sd}$) as 3 µl that was placed over the residue developed by the first droplet ($V_{fd}$). Furthermore, the advancing and receding contact angles were measured based on the tilting cradle method using tensiometer. Each experiment was performed three times on both residue and copper surfaces.

### *2.3. Droplet residue surface measurements*

The surface morphology (such as pore size and areal porosity) of the Cu-$Al_2O_3$ HNF droplet residue for all residue sizes was examined using a scanning electron microscopy technique (TM 3030, Hitachi, Japan). ImageJ software was used to post-process the SEM micrographs to obtain the areal porosity and mean pore (Feret) diameter at three distinct positions on a residue surface with maximum standard deviation of 0.276% and 0.061 µm, respectively. The optical profiler

(NPFLEX, Bruker, USA) was used to measure the roughness ratio ($a$) and average surface roughness of both residue and copper surfaces with highest standard deviation of 0.017 and 0.094 μm, respectively. Both roughness parameters were measured three times at different substrate locations. The surface free energy (solid-air interfacial tension) of copper and residue surfaces was measured using an optical tensiometer at three different locations by using water and diiodomethane as polar and dispersive solvents, respectively. The maximum standard deviation in surface free energy measurements was 1.979 mN/m.

## 3. Development of a new analytical model for the Cu-$Al_2O_3$ HNF droplet evaporation rate

A new analytical model is developed to estimate the Cu-$Al_2O_3$ HNF droplet evaporation rate on copper and residue surfaces. The schematics of an evaporating Cu-$Al_2O_3$ HNF droplet is illustrated in Fig. 1 (a). $R_1$ and $R_2$ are the radii of curvature of a sessile droplet and the concentration boundary layer [1,40,42], respectively, while $x_v(R_1)$ and $x_v(R_2)$ are the vapor mole fraction at radius of curvature $R_1$ and $R_2$, respectively. The concentration boundary layer ($R_2$) is the borderline around an evaporating droplet where the vapour concentration of an evaporating droplet is almost the same as the ambient vapour concentration. As the droplet evaporates, the vapor concentration varies along the radius of curvature $R$, from fully saturated vapor [$x_v(R_1) = P_{sat}/P_{atm}$] at the droplet-air interface ($R_1$) to partially saturated vapor [$x_v(R_2) = \varphi\, x_v(R_1)$] at the concentration boundary layer ($R_2$), where $R_1 \leq R \leq R_2$ and $\varphi = 0.3$. Our model is based on following assumptions:

1. As both the droplet and surrounding air are at thermal equilibrium and that evaporation is only based on mass diffusion, isothermal and quasi-steady state conditions are assumed in our model.

2. Water vapor and air, above the droplet, are assumed as a binary mixture of ideal gases.
3. The droplet is assumed as a spherical cap with its contact radius below the capillary length ($l_c = \sqrt{\gamma_{lv}/\rho g}$).
4. Mass diffusion from the droplet surface occurs in a stationary medium with negligible advection effects.
5. As evaporation occurs in a direction normal to the droplet surface, one-dimensional diffusion along the radius of curvature ($R$) is assumed [1], (as shown in Fig. 1 (a)).

Based on Fick's law, the droplet evaporation rate (in units of µl/s) is determined as [1]:

$$E = \frac{dV}{dt} = \frac{-MCD}{\rho}\left(\frac{dx_v}{dR}\right)(2\pi R^2 - 2\pi R R_1 cos\theta), \quad (1)$$

where $M$ is the molar mass of water, $C=P_{atm}/R_uT$ is the net molar concentration of a binary vapor-air mixture, $D$ is the mass diffusivity, $\rho$ is the density of water and $dx_v/dR$ is the vapor concentration gradient along the radius of curvature $R$. The last term in brackets in equation (1) is an area normal to the direction of evaporation that varies along the radius of curvature $R$ [1], as illustrated in Fig. 1 (b). As non-uniform evaporation (higher evaporation rate near the three-phase contact line than other regions on droplet surface) along the droplet surface leads to an outwardly driven flow (capillary flow) within the droplet to replenish the loss of evaporation near the three-phase contact line, it causes nanoparticles to deposit near the three-phase contact line resulting in a ring-shaped (coffee-ring) residue pattern [26,27]. Conversely, as we obtained a uniform residue pattern from the hybrid nanofluid droplet evaporation in all our experiments (as demonstrated in Fig. 1 (c-k)), the non-uniform evaporation along the droplet surface is not considered in our model. Moreover,

the developed model is a simplified 1-D model (assumption 5) in which the mass diffusion is only considered along the radius of curvature ($R$), therefore, it is the limitation of our proposed 1-D model that it does not consider the non-uniform evaporation rate along the droplet-air interface. As evaporation occurs at the droplet-air interface, the droplet evaporation rate ($E$) is independent of the radius of curvature ($R$) [1]. Re-arranging and integrating equation (1) gives the following form of the droplet evaporation rate:

$$\frac{E}{k}\int_{R1}^{R2}\left(\frac{1}{R^2-RR_1cos\theta}\right)dR = \int_{x_v(R_1)}^{x_v(R_2)} dx_v \,, \tag{2}$$

$$E = \frac{dV}{dt} = \frac{kR_1cos\theta[x_v(R_2)-x_v(R_1)]}{ln\left(\frac{1-(R_1/R_2)cos\theta}{1-cos\theta}\right)} \,. \tag{3}$$

where $k=-2\pi MCD/\rho$. Equation (3) gives the droplet evaporation rate ($E$) for any contact angle ($\theta$) during evaporation. Now, we determine the two unknown terms in equation (3). i.e., $R_1$ and $R_2$. $R_1$ can be determined as:

$$R_1 = \frac{r_{qe}}{sin\theta} \,, \tag{4}$$

where $r_{qe}$ is the droplet contact radius at a quasi-equilibrium state (when the droplet does not spread macroscopically [39]). The quasi-equilibrium contact radius ($r_{qe}$) in equation (4) is obtained from geometry of a spherical cap as:

$$r_{qe} = \left(\frac{3V_{sd}sin\theta_{qe}(1+cos\theta_{qe})}{\pi(2+cos\theta_{qe})(1-cos\theta_{qe})}\right)^{1/3}, \quad (5)$$

where $V_{sd}$ = 3 µl. It must be noted that the volume of the first droplet ($V_{fd}$) is not directly used in our model, as our model not only estimates the droplet evaporation rate over a residue surface but also over a copper surface (without a residue and does not involve $V_{fd}$). However, as $V_{fd}$ is only used to develop a residue and study its effect on evaporation rate of the second droplet, our model indirectly depends on $V_{fd}$ by means of its residue properties, such as the residue radius ($r_{res}$) and the roughness ratio ($a$), which are different for each considered volume of the first droplet ($V_{fd}$), as shown in Table 1. It must also be noted that the droplet quasi-equilibrium contact radius ($r_{qe}$) is the same as the residue radius for cases where the succeeding droplet spreads up to the residue boundary (i.e., $r_{qe} = r_{res}$). Thus, equation (5) is only used when the droplet quasi-equilibrium contact radius ($r_{qe}$) is less than the residue radius. i.e., the succeeding droplet does not spread up to the residue boundary. So, the residue size above which the succeeding droplet does not reach the residue boundary is defined as the critical residue size ($(V_{fd}/V_{sd})_c$). Therefore, equation (5) is used for cases where $V_{fd}/V_{sd} > (V_{fd}/V_{sd})_c$, while $r_{qe} = r_{res}$ for $V_{fd}/V_{sd} \leq (V_{fd}/V_{sd})_c$. The value of the critical residue size ($(V_{fd}/V_{sd})_c$) is obtained through experiments, as will be discussed in the next section (Results and discussion). $\theta_{qe}$ in equation (5) is a quasi-equilibrium contact angle and is determined as [45]:

$$\theta_{qe} = cos^{-1}(acos\theta_y), \quad (6)$$

where $a$ is the substrate roughness ratio (ratio of a textured area to projected area) and $\theta_y$ is the Young contact angle. As $r_{qe}$ is already known ($r_{qe} = r_{res}$) for $V_{fd}/V_{sd} \leq (V_{fd}/V_{sd})_c$, the quasi-equilibrium contact angle ($\theta_{qe}$) can be obtained from equation (5) instead of equation (6) for such

cases. The Young contact angle in equation (6) depends on interfacial tensions at the droplet three phase contact line and is given as [46]:

$$\theta_y = cos^{-1}\left(\frac{\gamma_{sv}-\gamma_{sl}}{\gamma_{lv}}\right), \quad (7)$$

The roughness ratio ($a$) in equation (6) and the surface free energy ($\gamma_{sv}$) in equation (7) were experimentally measured for both copper and the Cu-$Al_2O_3$ HNF residue surfaces, as shown in Table 1 and Table 2, respectively. In equation (7), the surface tension ($\gamma_{lv}$) for water and the Cu-$Al_2O_3$ HNF droplets was measured as 72.617±0.121 mN/m and 72.241±0.153 mN/m, respectively. Based on the OWRK/Fowkes theory, the solid-liquid interfacial tension ($\gamma_{sl}$) in equation (7) is determined as [47]:

$$\gamma_{sl} = \gamma_{sv} + \gamma_{lv} - 2\sqrt{\gamma_{sv}{}^{d}\gamma_{lv}{}^{d}} - 2\sqrt{\gamma_{sv}{}^{p}\gamma_{lv}{}^{p}}\ . \quad (8)$$

The measured values of polar and dispersive components of $\gamma_{sv}$ and $\gamma_{lv}$ used in equation (8) are shown in Table 2. Equations (4) to (8) are solved to determine the first unknown term ($R_1$) of the droplet evaporation equation (3). The vapor concentration gradient of an evaporating sessile droplet becomes negligibly small when the vapor concentration boundary layer $R_2$ is about 10 times the droplet contact radius $r_{qe}$ (i.e., $dx_v/dR \approx 0$ at $R_2 = 10r_{qe}$) [40,42], therefore, we use $R_2 = 10r_{qe}$ in our model. Since $r_{qe} = R_1 sin\theta$, we get the following expression for $R_2$:

$$R_2 = 10R_1 sin\theta \quad (9)$$

It must be noted that as the contact angle ($\theta$) reduces during the droplet evaporation, $R_1$ increases such that $R_2$ almost remains constant. The values of $R_1$ and $R_2$ from equations (4) and (9), respectively, are used in equation (3) to obtain the droplet evaporation rate for any given contact angle ($\theta$). Using equation (3), the net evaporation rate can be obtained as:

$$E_n = \left(\frac{dV}{dt}\right)_n = \frac{1}{\theta 1 - \theta 2}\int_{\theta 2}^{\theta 1} \frac{kR_1 cos\theta [x_v(R_2) - x_v(R_1)]}{ln\left(\frac{1-(R_1/R_2)cos\theta}{1-cos\theta}\right)} d\theta \quad (10)$$

where $\theta_1$ and $\theta_2$ are the droplet contact angles (in radians) at the start ($\theta_1 = \theta_{qe}$) and end of droplet evaporation process, respectively. As evaporation occurs at the droplet-air interface and that the main focus of our model is to estimate the hybrid nanofluid droplet evaporation rate, the hybrid nanoparticle deposition on substrate (droplet-solid interface) during the droplet evaporation is not directly considered in our model. However, as our model can only estimate the evaporation rate for pinned droplets and that the pinning effect in hybrid nanofluid droplets is induced by the hybrid nanoparticle deposition near the three-phase contact line during evaporation, therefore, our model in some way considers the effect of deposited hybrid nanoparticles during the droplet evaporation process.

## 4. Results and discussion

### *4.1. Effect of surface wettability and residue size on the Cu-$Al_2O_3$ HNF droplet evaporation rate*

The instantaneous variation of the Cu-$Al_2O_3$ HNF droplet volume sitting on copper and residue surfaces during evaporation is illustrated in Fig. 2 (a). The droplet volume ($V$) during evaporation is normalized with the initial (quasi-equilibrium) droplet volume ($V_i$). It is observed that the

evaporation time is almost the same for the Cu-$Al_2O_3$ HNF droplet resting on copper and its residue at $V_{fd}/V_{sd}$ = 0.5 and $V_{fd}/V_{sd}$ = 1. However, the evaporation time progressively decreases with increasing droplet volume ratio (residue size) from $V_{fd}/V_{sd}$ = 1 to $V_{fd}/V_{sd}$ = 2, 3, 4 and 5, resulting in a substantially reduced evaporation time (by about 64%) for $V_{fd}/V_{sd}$ = 5 as compared to $V_{fd}/V_{sd}$ = 0.5. Nonetheless, the evaporation time of the Cu-$Al_2O_3$ HNF droplet is not much affected by residue size for $V_{fd}/V_{sd}$ > 5, as shown in Fig. 2 (a). Furthermore, as shown in the inset of Fig. 2 (a), the evaporation time for a water droplet is 18% more than the Cu-$Al_2O_3$ HNF droplet resting on a copper surface. This is because the water droplet de-pins on a smooth copper surface during evaporation that reduces its droplet-air interfacial area (due to increase in contact angle) and consequently extends the net evaporation time. It is also noticed that our analytical model agrees well with the experimental data (average error of 8%) of the Cu-$Al_2O_3$ HNF droplet evaporation time.

Fig. 2 (b) shows that our analytical model estimates the droplet evaporation time with higher accuracy as compared to other existing models. Unlike our proposed analytical model, the other existing models [40–43] are approximate solutions depending on the droplet contact angle. The model proposed by Hu and Larson [40] is valid for the initial droplet contact angle ranging between 0° and 90°. Picknett and Bexon [41] proposed models for both constant contact radius and constant contact angle modes of droplet evaporation. Moreover, Hu et al. [42] showed with their developed model that the droplet evaporation rate is proportional to the droplet-air interfacial area. Although our semi-empirical model [39] well-estimates the Cu-$Al_2O_3$ hybrid nanofluid droplet evaporation time for droplets resting on a copper surface as well as the residue surface with small residue sizes ($V_{fd}/V_{sd}$ = 0.5-1), it shows deviations for large residue sizes (such as $V_{fd}/V_{sd}$ = 20), as shown in Fig.

2 (b). This is because the semi-empirical model was developed for the Ag-GNP hybrid nanofluid droplet [39] that showed different evaporation time for a range of wettability (highly wetted to non-wetted) of its residue surface depending upon the mixing ratio as compared to only partially wetted residue surface for the Cu-$Al_2O_3$ hybrid nanofluid droplet. On the other hand, the proposed analytical model (equation (3)) estimates the droplet evaporation time with higher accuracy for all residue sizes as compared to the semi-empirical model [39]. Since the evaporation rate ($dV/dt$) depends on the droplet contact angle ($\theta$) in all (proposed and existing) theoretical models, the droplet volume-time plot in Fig. 2 (a) and Fig. 2 (b) is obtained by solving these models at each time step with the known droplet contact angle from our experiments. Therefore, with the known initial droplet volume as 3 µl and droplet evaporation rate ($dV/dt$) determined from theoretical models at each time step, the droplet volume is obtained at each time step of the droplet evaporation process.

The net evaporation rate of 3 µl volume of water and Cu-$Al_2O_3$ HNF droplets is illustrated in Fig. 3 (a). It is noticed that the Cu-$Al_2O_3$ HNF droplet gives about 17% higher evaporation rate than a water droplet on a copper surface. Furthermore, the evaporation rate is almost the same for the Cu-$Al_2O_3$ HNF droplet sitting on a copper surface and residue surface, for droplet volume ratios of $V_{fd}/V_{sd} = 0.5$ and $V_{fd}/V_{sd} = 1$. However, further increasing the droplet volume ratio (droplet residue size) as $V_{fd}/V_{sd} = 2$, 3, 4 and 5 increases the evaporation rate of the succeeding Cu-$Al_2O_3$ HNF droplet on its residue by 31%, 59%, 76% and 106%, respectively, as compared to the droplet volume ratio of $V_{fd}/V_{sd} = 0.5$. This is because the succeeding Cu-$Al_2O_3$ HNF droplet spreads up to the boundary of a partially wetted residue surface with increasing residue size resulting in a large droplet-air interfacial area, as shown in Fig. 3 (b). Large droplet-air interfacial area allows more

406 water molecules to diffuse from the droplet surface into the air, which increases the droplet
407 evaporation rate. Conversely, droplets show negligible spreading over a non-wetted copper surface
408 and a residue surface for $V_{fd}/V_{sd}$ = 0.5 and $V_{fd}/V_{sd}$ = 1 (first three images in Fig. 3 (b)), resulting in
409 low droplet-air interfacial areas and reduced evaporation rates. Moreover, increasing the droplet
410 volume ratio above 5 (i.e., $V_{fd}/V_{sd}$ > 5) has a negligible effect on evaporation rate of succeeding
411 Cu-$Al_2O_3$ HNF droplets, as shown in Fig. 3 (a). This is because the droplets do not further spread
412 over their partially wetted residue surfaces for $V_{fd}/V_{sd}$ > 5 and exhibit almost the same droplet air
413 interfacial areas, as demonstrated in Fig. 3 (b). Moreover, the net droplet evaporation rate from
414 equation (10) agrees well with our experimental results (average error of 3.7%), as shown in Fig.
415 3 (a).
416
417 Fig. 4 (a) shows the variation of net evaporation rate and quasi-equilibrium droplet surface
418 area (or droplet-air interfacial area) of the Cu-$Al_2O_3$ HNF droplet with droplet residue size (droplet
419 volume ratio). It is noticed that the quasi-equilibrium droplet surface area linearly increases with
420 increasing residue size up to $V_{fd}/V_{sd}$ = 5, resulting in a linear increase in droplet evaporation rate.
421 However, the quasi-equilibrium droplet surface area as well as the evaporation rate almost remain
422 unchanged for residue size $V_{fd}/V_{sd}$ > 5, as shown in Fig. 4 (a). Therefore, $V_{fd}/V_{sd}$ = 5 is considered
423 as the critical residue size $(V_{fd}/V_{sd})_c$, as droplets do not further spread and give almost the same
424 droplet-air interfacial area and consequently the same evaporation rate above this critical value.
425 However, this critical value of $V_{fd}/V_{sd}$ = 5 for the Cu-$Al_2O_3$ hybrid nanofluid droplet over its residue
426 may be different for different hybrid nanofluid droplets over their respective residues. This is
427 because the critical residue size depends on the extent of droplet spreading over the residue surface

which is influenced by the residue surface characteristics (such as roughness and surface free energy) as well as the droplet rheological properties (such as viscosity and surface tension).

As already mentioned, the evaporation rate of the Cu-$Al_2O_3$ HNF droplet resting on its residue is not much affected above the critical residue size. i.e., $V_{fd}/V_{sd} > (V_{fd}/V_{sd})_c$. This is because the droplet contact radius and contact angle at quasi-equilibrium state almost remain unchanged (i.e., $\theta_{qe} = \theta_{qe,c} \approx 32°$ and $r_{qe} = r_{qe,c} \approx 1.64$ mm), as the droplet is un-bounded (does not reach the residue boundary) on a partially wetted residue for $V_{fd}/V_{sd} > (V_{fd}/V_{sd})_c$, as shown in Fig. 4 (b). Thus the quasi-equilibrium droplet-air interfacial area almost remains the same, resulting in similar droplet evaporation rates for $V_{fd}/V_{sd} > (V_{fd}/V_{sd})_c$. However, the Cu-$Al_2O_3$ HNF droplet is bounded (reaches the residue boundary) and does not spread beyond the residue boundary for residue size at or below its critical value. i.e., $V_{fd}/V_{sd} \leq (V_{fd}/V_{sd})_c$. In this region, the droplet contact radius and contact angle at quasi-equilibrium state show considerable variation, as shown in Fig. 4 (b). Therefore, our main interest lies in a residue size between $0 \leq V_{fd}/V_{sd} \leq (V_{fd}/V_{sd})_c$, where the Cu-$Al_2O_3$ HNF droplet evaporation rate varies by about 100%, as illustrated in Fig. 4 (a). It is further noticed that both the quasi-equilibrium contact angle and contact radius show linear variation with increasing residue size in a range of $0 \leq V_{fd}/V_{sd} \leq (V_{fd}/V_{sd})_c$, as demonstrated in Fig. 4 (b).

Fig. 5 (a) shows the net evaporation rate of 10 subsequent Cu-$Al_2O_3$ HNF droplets over the residue formed by evaporation of the first Cu-$Al_2O_3$ HNF droplet for residue sizes of $V_{fd}/V_{sd} = 2$ and $V_{fd}/V_{sd} = 6$. The reason for selecting these two residue sizes is that the subsequent droplet reaches the residue boundary for $V_{fd}/V_{sd} = 2$, while the subsequent droplet remains un-bounded (does not reach the residue boundary) for $V_{fd}/V_{sd} = 6$. In this way, the effect of residue boundary

451 on droplet evaporation rate is also incorporated along with the number of subsequent droplets. It
452 is observed that the droplet evaporation rate is not much affected by increasing the number of
453 subsequent droplets for the residue size of $V_{fd}/V_{sd}$ = 2. This is because all the 10 subsequent Cu-
454 $Al_2O_3$ HNF droplets reach the residue boundary of the first Cu-$Al_2O_3$ HNF droplet residue, thus
455 exhibiting almost the same droplet-air interfacial area and evaporation rate, as shown in Fig. 5 (a).
456 On the other hand, the droplet evaporation rate shows some variation with increasing number of
457 subsequent droplets over the residue surface for $V_{fd}/V_{sd}$ = 6. The reason for this variation in droplet
458 evaporation rate is that the subsequent droplets remain un-bounded and therefore show some
459 variation in spreading dynamics over the residue surface due to the contact angle hysteresis (about
460 6°). This results in slightly varying droplet-air interfacial areas as well as the evaporation rates for
461 subsequent droplets over the residue surface for $V_{fd}/V_{sd}$ = 6. However, the variation in evaporation
462 rate is not considerable for all 10 subsequent droplets over the residue surface for $V_{fd}/V_{sd}$ = 6.
463
464 Fig. 5 (b) shows the comparison of net evaporation rate and contact angle (at quasi-equilibrium
465 state) between the Cu-$Al_2O_3$ HNF droplet and the Ag-GNP (MR-1) HNF droplet [39] on copper
466 and their own residue surfaces. It should be noted that only mixing ratio MR-1 (0.1(Ag):0.9(GNP))
467 for the Ag-GNP HNF droplet is considered for comparison in this study, as it gave the highest
468 evaporation rate on its residue among all studied mixing ratios in our previous study [39]. In Fig.
469 5 (b), it is observed that both Cu-$Al_2O_3$ and Ag-GNP (MR-1) HNF droplets almost give same
470 evaporation rates on a copper surface and their own residue surfaces for $V_{fd}/V_{sd}$ = 1. However, the
471 Ag-GNP (MR-1) HNF droplet shows higher evaporation rate on its extremely wetted residue
472 surface than the Cu-$Al_2O_3$ HNF droplet on its partially wetted residue surface for $V_{fd}/V_{sd}$ > 5, as
473 demonstrated in Fig. 5 (b). This is because the Ag-GNP (MR-1) HNF droplet spreads on its

474 extremely wetted residue surface, giving a low (quasi-equilibrium) contact angle and large droplet-
475 air interfacial area that result in high evaporation rates. Conversely, the Cu-$Al_2O_3$ hybrid nanofluid
476 droplet does not further spread on its partially wetted residue surface for $V_{fd}/V_{sd} > 5$, resulting in
477 relatively large contact angle (small droplet-air interfacial area) and low evaporation rates, as
478 illustrated in Fig. 5 (b).
479

480 *4.2. Effect of surface wettability and residue size on the Cu-$Al_2O_3$ HNF droplet spreading*
481 *behaviour*

482 The contact angle variation of evaporating droplets is demonstrated in Fig. 6. Both water and
483 Cu-$Al_2O_3$ HNF droplets show a high quasi-equilibrium (initial) contact angle of $\theta_{qe} \approx 104°$ on a
484 non-wetted copper surface and exhibit a similar trend of contact angle reduction rate. However,
485 the evaporating water droplet undergoes a de-pinning effect that extends its total evaporation time.
486 On the other hand, the Cu-$Al_2O_3$ HNF droplet remains pinned due to the deposition of hybrid
487 nanoparticles near the droplet three-phase contact line during its evaporation. For droplet volume
488 ratios of $V_{fd}/V_{sd} = 0.5$ and $V_{fd}/V_{sd} = 1$, the Cu-$Al_2O_3$ HNF droplet resting on a residue surface almost
489 shows the same contact angle reduction rate as the one resting on a copper surface, as illustrated
490 in Fig. 6. The quasi-equilibrium contact angle gradually decreases with increasing droplet volume
491 ratio as $V_{fd}/V_{sd} = 2$, 3, 4 and 5, resulting in significant reduction in quasi-equilibrium contact angle
492 by 69% at the critical droplet volume ratio $(V_{fd}/V_{sd})_c$ as compared to $V_{fd}/V_{sd} = 0.5$. Furthermore, the
493 timely variation of contact angle shows a non-linear trend for $V_{fd}/V_{sd} \leq 2$ compared to a linear trend
494 for $V_{fd}/V_{sd} > 2$. For droplet volume ratio $V_{fd}/V_{sd} > (V_{fd}/V_{sd})_c$, the contact angle (quasi-equilibrium)
495 of the succeeding Cu-$Al_2O_3$ HNF droplet remains unaffected, exhibiting nearly the same contact
496 angle reduction rate. For this reason, the Cu-$Al_2O_3$ HNF droplet almost gives the same evaporation

rate on a residue surface for droplet volume ratio $V_{fd}/V_{sd} > (V_{fd}/V_{sd})_c$. Furthermore, the advancing and receding contact angles (dynamic contact angle) for the Cu-$Al_2O_3$ hybrid nanofluid droplet are 109.81° and 100.34° on a copper surface and 34.44° and 28.79° on a residue surface (for $V_{fd}/V_{sd} > (V_{fd}/V_{sd})_c$), respectively. The contact angle hysteresis of the Cu-$Al_2O_3$ hybrid nanofluid droplet on both residue and plain copper surfaces may be induced by the deposition of hybrid nanoparticles near the droplet three-phase contact line. Since the contact angle hysteresis is observed for Cu-$Al_2O_3$ HNF droplets resting on both residue and plain copper surfaces, the evaporation enhancement for droplets resting on residue surfaces may not be attributed to the dynamic (advancing and receding) contact angle.

Fig. 7 shows the instantaneous variation of contact radius of evaporating droplets. As the surface tension of water and Cu-$Al_2O_3$ HNF droplets is almost the same, both these droplets show similar quasi-equilibrium contact radius on a copper surface. However, the contact radius is sharply reduced in an evaporating water droplet on a copper surface due to the de-pinning effect for time above 900 seconds. On the other hand, for Cu-$Al_2O_3$ HNF droplets resting on both copper and residue surfaces, the contact radius remains constant during most part of the total evaporation time, as shown in Fig. 7. This is because the hybrid nanoparticles deposit during the droplet evaporation thus resulting in a pinning effect for Cu-$Al_2O_3$ HNF droplets sitting on copper and residue surfaces. Furthermore, the Cu-$Al_2O_3$ HNF droplet nearly shows the same contact radius on copper and residue surfaces for droplet volume ratios of $V_{fd}/V_{sd} = 0.5$ and $V_{fd}/V_{sd} = 1$. However, the contact radius increases by 30%, 42%, 63% and 70% for droplet volume ratio of $V_{fd}/V_{sd} = 2$, 3, 4 and 5, respectively, as compared to the droplet volume ratio of $V_{fd}/V_{sd} = 0.5$. This is because the succeeding Cu-$Al_2O_3$ HNF droplet spreads up to the boundary of its partially wetted residue

surface resulting in a large contact radius with increasing residue size up to $(V_{fd}/V_{sd})_c$. Moreover, further increasing the droplet volume ratio as $V_{fd}/V_{sd} > (V_{fd}/V_{sd})_c$ does not much affect the contact radius of the succeeding Cu-$Al_2O_3$ HNF droplet on its residue surface. This is for the reason that the succeeding Cu-$Al_2O_3$ HNF droplet is unbounded for $V_{fd}/V_{sd} > (V_{fd}/V_{sd})_c$ and its spreading over the residue surface is governed by residue surface characteristics, such as the residue roughness and surface free energy, as discussed in the next section.

### *4.3. Effect of residue morphology, surface free energy and roughness on the Cu-$Al_2O_3$ HNF droplet wetting and evaporation rate*

The surface morphology for various sizes of the Cu-$Al_2O_3$ HNF droplet residue is illustrated in SEM micrographs in Fig. 8. The residue surface appears rough and porous, making it difficult to distinguish between Cu and $Al_2O_3$ nanoparticles on a residue surface. Although hybrid nanoparticles deposit uniformly during evaporation leaving a uniform pattern of nanostructured residue, some large clustered particles are observed in SEM micrographs, as identified by circles in Fig. 8. These clustered particles are possibly formed by hybrid nanoparticle agglomeration due to increase in particle concentration with the progression of droplet evaporation process. The average surface roughness and areal porosity increase as the residue size increases, as shown in Table 1. The main reason for increase in average surface roughness and porosity is the increase in residue surface particle density ($\rho_{res}$) with increasing residue size, as shown in Table 1. The residue surface particle density is determined as the net volume of deposited hybrid nanoparticles (determined as 0.1% of droplet volume, as volume fraction is fixed at 0.1%) per unit residue area. As the residue size increases, the net particle volume per unit residue area also increases that results in its increasing surface roughness and porosity. Furthermore, the average surface roughness of

Cu-$Al_2O_3$ HNF droplet residues is 16-50 times that of a copper surface. High residue roughness promotes droplet spreading, resulting in high droplet evaporation rates. Another important parameter that promotes droplet wetting is the surface free energy, which is 25.4% higher in the Cu-$Al_2O_3$ HNF droplet residue surface than the plain copper surface, as shown in Table 2. As the surface free energy is a surface property and is independent of residue size, we measured it at a high droplet volume ratio of $V_{fd}/V_{sd} = 20$ (as shown in Table 2), ensuring that the succeeding droplet is un-bounded and does not reach the residue boundary. Moreover, the roughness ratio ($a$), which is the ratio of the actual textured area to the projected (plain) area [48], is up to 70% higher for the Cu-$Al_2O_3$ HNF droplet residue than the copper surface, as shown in Table 1. It is suggested that the surface roughness and porosity of the droplet residue increase its textured area thus giving a high roughness ratio. The combined effect of both, high roughness ratio and enhanced surface free energy, increase the wettability of the Cu-$Al_2O_3$ HNF droplet residue surface. This promotes spreading resulting in high evaporation rate of the succeeding Cu-$Al_2O_3$ HNF droplet resting over its residue surface, which is not the case with non-wetted copper surface, as shown in Table 2.

## 5. Conclusions

High heat dissipation in high heat flux devices is increasingly becoming a challenge, mainly due to the limited cooling capacity of existing thermal fluids. To address this challenge, we studied the evaporation rate of Cu-$Al_2O_3$ HNF droplets and compared with water droplets on a copper surface at room temperature. Subsequently, we investigated the effect of residue formed after the evaporation of the first Cu-$Al_2O_3$ HNF droplet, on the evaporation rate of the succeeding Cu-$Al_2O_3$ HNF droplet, for residue sizes above and below the critical residue size. As the main novelty, we showed that the evaporation rate of the succeeding Cu-$Al_2O_3$ HNF droplet resting over the residue

566 sharply increases with increasing residue size up to the critical residue size. Furthermore, the
567 evaporation rate of the succeeding droplet almost remains the same as the residue size is further
568 increased above the critical residue size. We also noticed that the evaporation rate of the
569 succeeding Cu-$Al_2O_3$ HNF droplet resting over the partially wetted large sized residue is
570 considerably higher than the one sitting on a non-wetted copper surface. Moreover, we developed
571 a new analytical model that can estimate the evaporation rate of the Cu-$Al_2O_3$ HNF droplet over a
572 wide contact angle range. Furthermore, we also studied the effect of the residue surface free energy
573 and its roughness on wetting and evaporation rate of the Cu-$Al_2O_3$ HNF droplet sitting over the
574 residue surface. The main conclusions of this study are as follows:
575

576 • The evaporation rate of the Cu-$Al_2O_3$ HNF droplet is 17% higher than that of a water
577 droplet resting on a copper surface.
578 • The evaporation rate of the Cu-$Al_2O_3$ HNF droplet on its residue surface is enhanced up
579 to 104% when compared to a copper surface.
580 • The evaporation rate of the Cu-$Al_2O_3$ HNF droplet on its residue surface increases by 6%,
581 31%, 59%, 76% and 106% for droplet volume ratio of $V_{fd}/V_{sd}$ =1, 2, 3, 4 and 5,
582 respectively, as compared to the droplet volume ratio of $V_{fd}/V_{sd}$ = 0.5.
583 • The Cu-$Al_2O_3$ HNF droplet evaporation rate on a residue surface almost remains the same
584 for $V_{fd}/V_{sd} > (V_{fd}/V_{sd})_c$.
585 • The quasi-equilibrium contact angle of the Cu-$Al_2O_3$ HNF droplet over its residue reduces
586 by 70% while the quasi-equilibrium contact radius increases by 70%, as the droplet
587 volume ratio increases from $V_{fd}/V_{sd}$ = 0.5 to $(V_{fd}/V_{sd})_c$.

- The average surface roughness of the Cu-$Al_2O_3$ HNF droplet residues is 16-50 times that of a copper surface.
- The surface free energy and roughness ratio of the Cu-$Al_2O_3$ HNF droplet residue is 25.4% and 70% higher than that of a copper surface, respectively.

**Acknowledgments**

The funding for this research is provided by the Hong Kong PhD Fellowship Scheme (HKPFS), the Hong Kong Research Grant Council via Collaborative Research Fund (CRF) account C6022-16G, General Research Fund (GRF) account 16206918 and Early Career Scheme (ECS) account 21200819.

**Nomenclature**

| | | | |
|---|---|---|---|
| $a$ | Roughness ratio | $V_{fd}$ | Volume of first droplet, µl |
| $C$ | Net molar concentration, $molm^{-3}$ | $V_{fd}/V_{sd}$ | Droplet volume ratio |
| $D$ | Mass diffusivity, $m^2s^{-1}$ | $(V_{fd}/V_{sd})_c$ | Critical residue size |
| $E$ | Droplet evaporation rate, $\mu ls^{-1}$ | $x_v$ | Vapor mole fraction |
| $E_n$ | Net droplet evaporation rate, $\mu ls^{-1}$ | *Greek Letters* | |
| $g$ | Gravitational constant, $ms^{-2}$ | $\rho$ | Density, $kgm^{-3}$ |
| *HNF* | Hybrid nanofluid | $\rho_{res}$ | Residue surface particle density, $\mu lmm^{-2}$ |
| $l_c$ | Capillary length, m | $\gamma_{lv}$ | Surface tension, $mNm^{-1}$ |
| $M$ | Molar mass, $gmol^{-1}$ | $\gamma_{lv}{}^p$ | Polar surface tension, $mNm^{-1}$ |
| $MR$ | Mixing ratio | $\gamma_{lv}{}^d$ | Dispersive surface tension, $mNm^{-1}$ |
| $P_{atm}$ | Atmospheric pressure, Pa | $\gamma_{sv}$ | Surface free energy, $mNm^{-1}$ |
| $P_{sat}$ | Saturation vapor pressure, Pa | $\gamma_{sv}{}^p$ | Polar surface free energy, $mNm^{-1}$ |
| $R$ | Radius of curvature, m | $\gamma_{sv}{}^d$ | Dispersive surface free energy, $mNm^{-1}$ |
| $R_u$ | Universal gas constant, $Jmol^{-1}K^{-1}$ | $\gamma_{sl}$ | Solid-liquid interfacial tension, $mNm^{-1}$ |

| | | | |
|---|---|---|---|
| $r$ | Contact radius, m | $\varphi$ | Relative humidity |
| $r_{qe}$ | Quasi-equilibrium contact radius, m | $\theta$ | Contact angle |
| $r_{qe,c}$ | Critical quasi-equilibrium contact radius, m | $\theta_y$ | Young contact angle |
| $r_{res}$ | Droplet residue radius, m | $\theta_{qe}$ | Quasi-equilibrium contact angle |
| $T$ | Temperature, K | $\theta_{qe,c}$ | Critical quasi-equilibrium contact angle |
| $V_{sd}$ | Volume of second droplet, µl | | |

## References


[1] Incropera, F. P., DeWitt, D. P., Bergman, T. L., and Lavine, A. S., 2007, *Fundamentals of Heat and Mass Transfer*, John Wiley and Sons.

[2] "Critical Heat Flux" [Online]. Available: https://en.wikipedia.org/wiki/Critical_heat_flux. [Accessed: 21-Jul-2020].

[3] Sung, M. K., and Mudawar, I., 2009, "Single-Phase and Two-Phase Hybrid Cooling Schemes for High-Heat-Flux Thermal Management of Defense Electronics," *Journal of Electronic Packaging*, **131**(2).

[4] Tso, C. Y., and Chao, C. Y. H., 2015, "Study of Enthalpy of Evaporation, Saturated Vapor Pressure and Evaporation Rate of Aqueous Nanofluids," *International Journal of Heat and Mass Transfer*, **84**, pp. 931–941.

[5] Fu, S., Tso, C., Fong, Y., and Chao, C. Y. H., 2017, "Evaporation of Al2O3-Water Nanofluids in an Externally Micro-Grooved Evaporator," *Science and Technology for the Built Environment*, **23**(2), pp. 345–354.

[6] Tso, C. Y., Fu, S. C., and Chao, C. Y. H., 2014, "A Semi-Analytical Model for the Thermal Conductivity of Nanofluids and Determination of the Nanolayer Thickness," *International Journal of Heat and Mass Transfer*, **70**, pp. 202–214.

[7] Akilu, S., Sharma, K. V., Baheta, A. T., and Mamat, R., 2016, "A Review of Thermophysical Properties of Water Based Composite Nanofluids," *Renewable and Sustainable Energy Reviews*, **66**, pp. 654–678.

[8] Sefiane, K., and Bennacer, R., 2009, "Nanofluids Droplets Evaporation Kinetics and Wetting Dynamics on Rough Heated Substrates," *Advances in Colloid and Interface Science*, **147**–**148**, pp. 263–271.

[9] Kim, Y. C., 2015, "Evaporation of Nanofluid Droplet on Heated Surface," *Advances in Mechanical Engineering*, **7**(4), pp. 1–8.

[10] Liang, G., and Mudawar, I., 2017, "Review of Spray Cooling – Part 1: Single-Phase and Nucleate Boiling Regimes, and Critical Heat Flux," *International Journal of Heat and Mass Transfer*, **115**, pp. 1174–1205.

[11] Sakashita, H., 2016, "Pressure Effect on CHF Enhancement in Pool Boiling of Nanofluids," *Journal of Nuclear Science and Technology*, **53**(6), pp. 797–802.

[12] Song, S. L., Lee, J. H., and Chang, S. H., 2014, "CHF Enhancement of SiC Nanofluid in Pool Boiling Experiment," *Experimental Thermal and Fluid Science*, **52**, pp. 12–18.

[13] Babu, J. A. R., Kumar, K. K., and Rao, S. S., 2017, "State-of-Art Review on Hybrid Nanofluids," *Renewable and Sustainable Energy Reviews*, **77**(April), pp. 551–565.

[14] Nine, M. J., Chung, H., Tanshen, M. R., Osman, N. A. B. A., and Jeong, H., 2014, "Is Metal Nanofluid Reliable as Heat Carrier?," *Journal of Hazardous Materials*, **273**, pp. 183–191.

[15] Sarkar, J., Ghosh, P., and Adil, A., 2015, "A Review on Hybrid Nanofluids: Recent Research, Development and Applications," *Renewable and Sustainable Energy Reviews*, **43**, pp. 164–177.

[16] Siddiqui, F. R., Tso, C. Y., Chan, K. C., Fu, S. C., and Chao, C. Y. H., 2019, "On Trade-off for Dispersion Stability and Thermal Transport of Cu-Al2O3 Hybrid Nanofluid for Various Mixing Ratios," *International Journal of Heat and Mass Transfer*, **132**, pp. 1200–1216.

[17] Batmunkh, M., Tanshen, M. R., Nine, M. J., Myekhlai, M., Choi, H., and Chung, H., 2014, "Thermal Conductivity of TiO2 Nanoparticles Based Aqueous Nanofluids with an Addition of a Modified Silver Particle," *Industrial & Engineering Chemistry Research*, **53**(20), pp. 8445–8451.

[18] Nine, M. J., Batmunkh, M., Kim, J.-H., Chung, H.-S., and Jeong, H.-M., 2012,

"Investigation of Al2O3-MWCNTs Hybrid Dispersion in Water and Their Thermal Characterization," *Journal of nanoscience and nanotechnology*, **12**, pp. 4553–4559.

[19] Han, Z. H, Yang, B., Kim, S. H., Zachariah, M. R., 2007, "Application of Hybrid Sphere/Carbonnanotube Particles in Nanofluids," *Nanotechnology*, **18**(10), pp. 105–109.

[20] Siddiqui, F. R., Tso, C. Y., Fu, S. C., Chao, C. Y. H., and Qiu, H. H., "Experimental Investigation On Silver-Graphene Hybrid Nanofluid Droplet Evaporation And Wetting Characteristics Of Its Nanostructured Droplet Residue," *Proceedings of the ASME-JSME-KSME 2019 8th Joint Fluids Engineering Conference. Volume 4: Fluid Measurement and Instrumentation; Micro and Nano Fluid Dynamics.*, San Francisco, California, USA. July 28–August 1, 2019.

[21] Hemmat Esfe, M., Abbasian Arani, A. A., Rezaie, M., Yan, W.-M., and Karimipour, A., 2015, "Experimental Determination of Thermal Conductivity and Dynamic Viscosity of Ag–MgO/Water Hybrid Nanofluid," *International Communications in Heat and Mass Transfer*, **66**, pp. 189–195.

[22] Yarmand, H., Gharehkhani, S., Ahmadi, G., Shirazi, S. F. S., Baradaran, S., Montazer, E., Zubir, M. N. M., Alehashem, M. S., Kazi, S. N., and Dahari, M., 2015, "Graphene Nanoplatelets–Silver Hybrid Nanofluids for Enhanced Heat Transfer," *Energy Conversion and Management*, **100**, pp. 419–428.

[23] Baghbanzadeh, M., Rashidi, A., Rashtchian, D., Lotfi, R., and Amrollahi, A., 2012, "Synthesis of Spherical Silica/Multiwall Carbon Nanotubes Hybrid Nanostructures and Investigation of Thermal Conductivity of Related Nanofluids," *Thermochimica Acta*, **549**, pp. 87–94.

[24] Hemmat Esfe, M., Alirezaie, A., and Rejvani, M., 2017, "An Applicable Study on the Thermal Conductivity of SWCNT-MgO Hybrid Nanofluid and Price-Performance Analysis for Energy Management," *Applied Thermal Engineering*, **111**, pp. 1202–1210.

[25] Siddiqui, F. R., Tso, C. Y., Fu, S. C., Qiu, H., and Chao, C. Y. H., "Evaporation of Silver-Graphene Hybrid Nanofluid Droplet on Its Nanostructured Residue and Plain Copper Surfaces at Elevated Temperatures," *Proceedings of the ASME 2020 Heat Transfer Summer*

*Conference Collocated with the ASME 2020 Fluids Engineering Division Summer Meeting and the ASME 2020 18th International Conference on Nanochannels, Microchannels, and Minichannels.*, Virtual, Online. July 13–15, 2020.

[26] Deegan, R. D., Bakajin, O., Dupont, T. F., Huber, G., Nagel, S. R., and Witten, T. A., 2000, "Contact Line Deposits in an Evaporating Drop," *Physical Review E*, **62**(1), pp. 756–765.

[27] Deegan, R. D., 2000, "Pattern Formation in Drying Drops," *Physical Review E - Statistical Physics, Plasmas, Fluids, and Related Interdisciplinary Topics*, **61**(1), pp. 475–485.

[28] Wang, F.-C., and Wu, H.-A., 2013, "Pinning and Depinning Mechanism of the Contact Line during Evaporation of Nano-Droplets Sessile on Textured Surfaces," *Soft Matter*, **9**(24), pp. 5703–5709.

[29] Moghiman, M., and Aslani, B., 2013, "Influence of Nanoparticles on Reducing and Enhancing Evaporation Mass Transfer and Its Efficiency," *International Journal of Heat and Mass Transfer*, **61**, pp. 114–118.

[30] Chen, R.-H., Phuoc, T. X., and Martello, D., 2010, "Effects of Nanoparticles on Nanofluid Droplet Evaporation," *International Journal of Heat and Mass Transfer*, **53**(19), pp. 3677–3682.

[31] Radiom, M., Yang, C., and Chan, W. K., 2013, "Dynamic Contact Angle of Water-Based Titanium Oxide Nanofluid," *Nanoscale Research Letters*, **8**(1), p. 282.

[32] Hong, S. J., Chou, T. H., Liu, Y. Y., Sheng, Y. J., and Tsao, H. K., 2013, "Advancing and Receding Wetting Behavior of a Droplet on a Narrow Rectangular Plane," *Colloid and Polymer Science*, **291**(2), pp. 347–353.

[33] Zhong, X., Crivoi, A., and Duan, F., 2015, "Sessile Nanofluid Droplet Drying," *Advances in Colloid and Interface Science*, **217**, pp. 13–30.

[34] Zhang, C., Zhu, X., and Zhou, L., 2011, "Morphology Tunable Pinning Force and Evaporation Modes of Water Droplets on PDMS Spherical Cap Micron-Arrays," *Chemical Physics Letters*, **508**(1), pp. 134–138.

[35] Craster, R. V, Matar, O. K., and Sefiane, K., 2009, "Pinning, Retraction, and Terracing of

703 Evaporating Droplets Containing Nanoparticles," *Langmuir*, **25**(6), pp. 3601–3609.

704 [36] Yunker, P. J., Still, T., Lohr, M. A., and Yodh, A. G., 2011, "Suppression of the Coffee-
705 Ring Effect by Shape-Dependent Capillary Interactions," *Nature*, **476**(7360), pp. 308–311.

706 [37] Lee, H. H., Fu, S. C., Tso, C. Y., and Chao, C. Y. H., 2017, "Study of Residue Patterns of
707 Aqueous Nanofluid Droplets with Different Particle Sizes and Concentrations on Different
708 Substrates," *International Journal of Heat and Mass Transfer*, **105**, pp. 230–236.

709 [38] Bigioni, T. P., Lin, X.-M., Nguyen, T. T., Corwin, E. I., Witten, T. A., and Jaeger, H. M.,
710 2006, "Kinetically Driven Self Assembly of Highly Ordered Nanoparticle Monolayers,"
711 *Nature Materials*, **5**(4), pp. 265–270.

712 [39] Siddiqui, F. R., Tso, C. Y., Fu, S. C., Qiu, H. H., and Chao, C. Y. H., 2020, "Evaporation
713 and Wetting Behavior of Silver-Graphene Hybrid Nanofluid Droplet on Its Porous Residue
714 Surface for Various Mixing Ratios," *International Journal of Heat and Mass Transfer*, **153**,
715 p. 119618.

716 [40] Hu, H., and Larson, R. G., 2002, "Evaporation of a Sessile Droplet on a Substrate," *The*
717 *Journal of Physical Chemistry B*, **106**, pp. 1334–1344.

718 [41] Picknett, R. G., and Bexon, R., 1977, "The Evaporation of Sessile or Pendant Drops in Still
719 Air," *Journal of Colloid and Interface Science*, **61**(2), pp. 336–350.

720 [42] Hu, D., Wu, H., and Liu, Z., 2014, "Effect of Liquid-Vapor Interface Area on the
721 Evaporation Rate of Small Sessile Droplets," *International Journal of Thermal Sciences*,
722 **84**, pp. 300–308.

723 [43] Popov, Y. O., 2005, "Evaporative Deposition Patterns : Spatial Dimensions of the Deposit,"
724 *Physical Review E*, **71**(August 2004), pp. 1–17.

725 [44] Siddiqui, F. R., Tso, C. Y., Chan, K. C., Fu, S. C., and Chao, C. Y. H., 2019, "Dataset on
726 Critical Parameters of Dispersion Stability of Cu/Al2O3 Nanofluid and Hybrid Nanofluid
727 for Various Ultra-Sonication Times," *Data in Brief*, **22**, pp. 863–865.

728 [45] Wenzel, R. N., 1936, "Resistance of Solid Surfaces to Wetting by Water," *Industrial and*
729 *Engineering Chemistry*, **28**(8), pp. 988–994.

730 [46] Young, T., 1805, "An Essay on the Cohesion of Fluids," *Philosophical Transactions of the*
731 *Royal Society of London*, **95**, pp. 65–87.

732 [47] Fowkes, F. M., 1964, "Attractive Forces at Interfaces," *Industrial & Engineering*
733 *Chemistry*, **56**(12), pp. 40–52.

734 [48] "Roughness Ratio" [Online]. Available:
735 https://www.biolinscientific.com/measurements/surface-roughness. [Accessed: 22-Jul-
736 2020].

737 [49] "Micropipettes" [Online]. Available: https://www.thermofisher.com/hk/en/home/life-
738 science/lab-plasticware-supplies/pipettes-pipette-tips/single-channel-pipettes.html.
739 [Accessed: 05-Aug-2020].

740

## List of Figure Captions

Fig. 1 (a) Schematics of an evaporating Cu-$Al_2O_3$ hybrid nanofluid droplet with suspended (grey) nanoparticles, (b) illustration of an area corresponding to the radius of curvature *R* and normal to the direction of evaporation (used in equation (1)), (c-k) microscopic images of Cu-$Al_2O_3$ HNF droplet residues obtained from droplet volumes ($V_{fd}$) of (c) 1.5 µl, (d) 3 µl, (e) 6 µl, (f) 9 µl, (g) 12 µl, (h) 15 µl, (i) 18 µl, (j) 30 µl and (k) 60 µl.

Fig. 2 (a) Instantaneous variation of droplet volume (empty circles (experiments), solid lines (analytical model/equation (3)) for the Cu-$Al_2O_3$ HNF droplet resting on a copper surface (Cu (HNF)) and on residue of various sizes ($V_{fd}/V_{sd}$ = 0.5-20). Inset is a comparison of $H_2O$ and the Cu-$Al_2O_3$ HNF droplet evaporation time on a copper surface, (b) comparison of theoretical models ((——— ) equation (3)), (— — —) Siddiqui et al. [39], (.....) Hu and Larson [40], (- - - - -) Picknett and Bexon [41] and (— · — ·) Hu et al. [42]) with our experimental results (empty circles) for the Cu-$Al_2O_3$ HNF droplet evaporation.

Fig. 3 (a) Net evaporation rate of water droplet over a copper surface (Cu ($H_2O$)) and the Cu-$Al_2O_3$ HNF droplet over a copper (Cu (HNF)) and its residue surface for various residue sizes ($V_{fd}/V_{sd}$ = 0.5-20), (b) Cu-$Al_2O_3$ HNF droplet images at quasi-equilibrium state resting on copper (Cu (HNF)) and residue surfaces ($V_{fd}/V_{sd}$ = 0.5-20).

Fig. 4 (a) Variation of the Cu-$Al_2O_3$ HNF net droplet evaporation rate and quasi-equilibrium droplet surface area (droplet-air interfacial area) with droplet volume ratio, (b) variation of droplet contact angle and contact radius at quasi-equilibrium state with droplet volume ratio. $V_{fd}/V_{sd}$ = 0 refers to the Cu-$Al_2O_3$ HNF droplet resting on a copper surface.

Fig. 5 (a) Net evaporation rate for subsequent Cu-$Al_2O_3$ hybrid nanofluid droplets over the residue formed by the first evaporated droplet, (b) comparison of net evaporation rate and the quasi-

764 equilibrium contact angle of Cu-$Al_2O_3$ hybrid nanofluid and Ag-GNP/MR-1 hybrid nanofluid [39]
765 droplets over copper and their respective residue surfaces.

766 Fig. 6 Contact angle variation of water droplet on a copper surface (Cu ($H_2O$)) and the Cu-$Al_2O_3$
767 HNF droplet on copper (Cu (HNF)) and residue surfaces ($V_{fd}/V_{sd}$ = 0.5-20) with time.

768 Fig. 7 Contact radius variation of water droplet on a copper surface (Cu ($H_2O$)) and the Cu-$Al_2O_3$
769 HNF droplet on copper (Cu (HNF)) and residue surfaces ($V_{fd}/V_{sd}$ = 0.5-20) with time.

770 Fig. 8 SEM micrographs of Cu-$Al_2O_3$ HNF droplet residues obtained from droplet volumes ($V_{fd}$)
771 of (a) 1.5 µl, (b) 3 µl, (c) 6 µl, (d) 9 µl, (e) 12 µl, (f) 15 µl, (g) 18 µl, (h) 30 µl and (i) 60 µl. Circles
772 show the presence of clustered hybrid nanoparticles on residue surfaces.

773

774

775 **List of Table Captions**

776 Table 1 Copper and the Cu-$Al_2O_3$ HNF droplet residue surface characteristics. Uncertainties for

777 first droplet volume ($V_{fd}$) are obtained from manufacturer [49].

778 Table 2 Surface free energy of substrates and its effect on wetting and evaporation rate of the Cu-

779 $Al_2O_3$ HNF droplet.

780

781

782

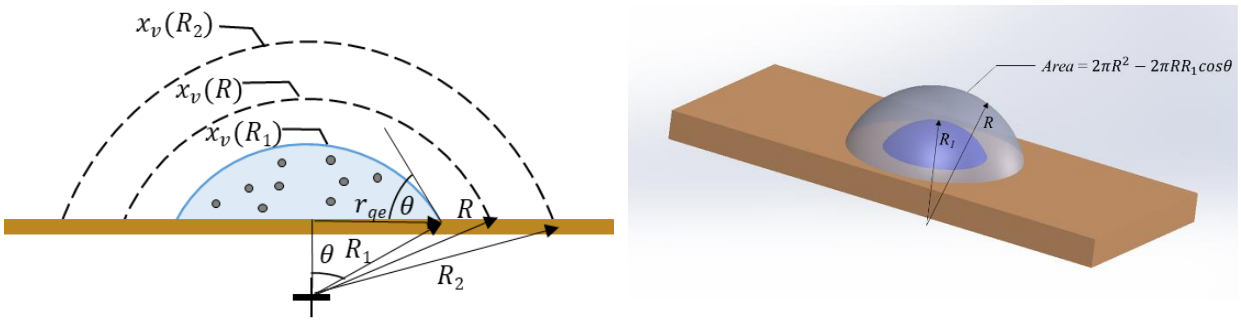


(a) (b)

783

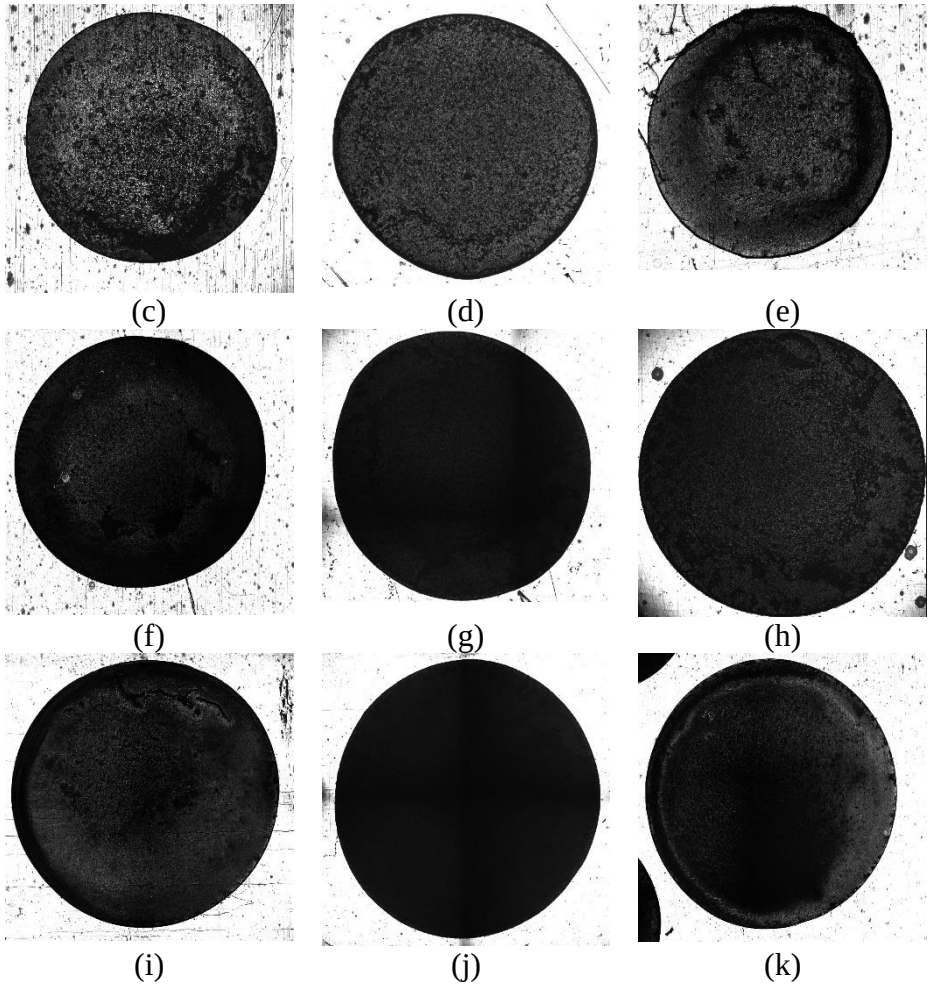

(c) (d) (e)

(f) (g) (h)

(i) (j) (k)

784 Fig. 1 (a) Schematics of an evaporating Cu-$Al_2O_3$ hybrid nanofluid droplet with suspended (grey)
785 nanoparticles, (b) illustration of an area corresponding to the radius of curvature *R* and normal to
786 the direction of evaporation (used in equation (1)), (c-k) microscopic images of Cu-$Al_2O_3$ HNF
787 droplet residues obtained from droplet volumes ($V_{fd}$) of (c) 1.5 µl, (d) 3 µl, (e) 6 µl, (f) 9 µl, (g)
788 12 µl, (h) 15 µl, (i) 18 µl, (j) 30 µl and (k) 60 µl.

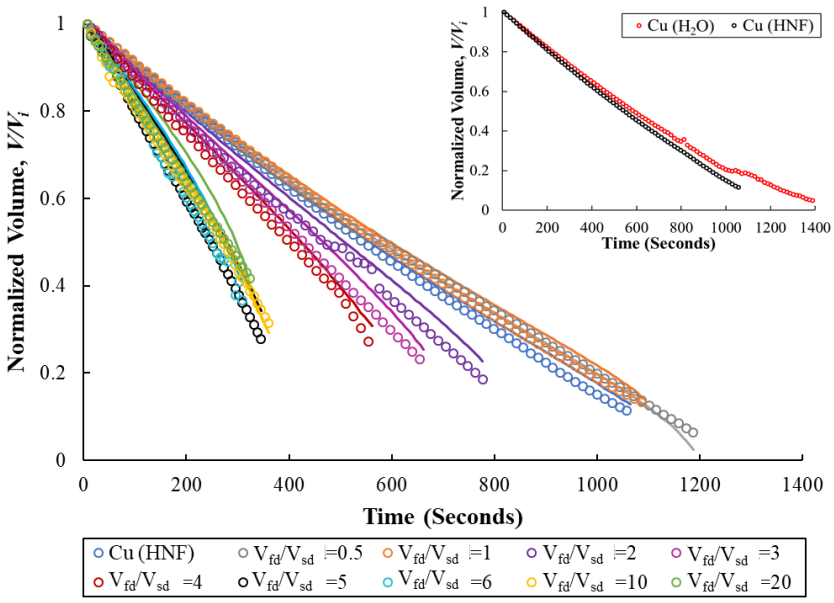


(a)

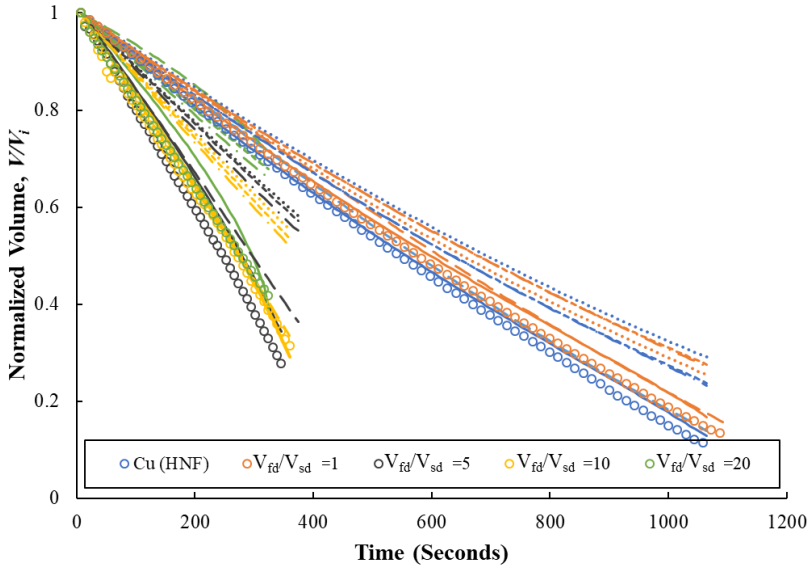


(b)

Fig. 2 (a) Instantaneous variation of droplet volume (empty circles (experiments), solid lines (analytical model/equation (3)) for the Cu-$Al_2O_3$ HNF droplet resting on a copper surface (Cu (HNF)) and on residue of various sizes ($V_{fd}/V_{sd}$ = 0.5-20). Inset is a comparison of $H_2O$ and the Cu-$Al_2O_3$ HNF droplet evaporation time on a copper surface, (b) comparison of theoretical models ((———— ) equation (3)), (— — —) Siddiqui et al. [39], (.....) Hu and Larson [40], ( ------) Picknett and Bexon [41] and (— · — ·) Hu et al. [42]) with our experimental results (empty circles) for the Cu-$Al_2O_3$ HNF droplet evaporation.

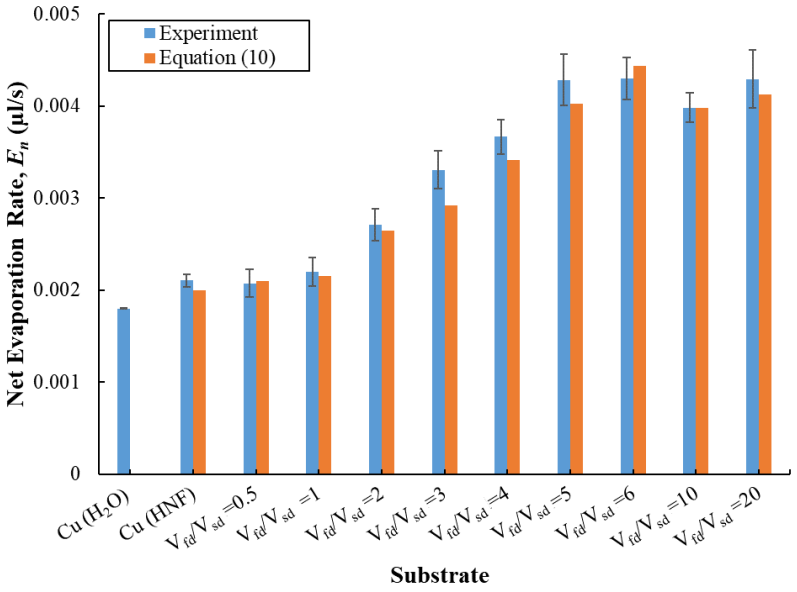


(a)

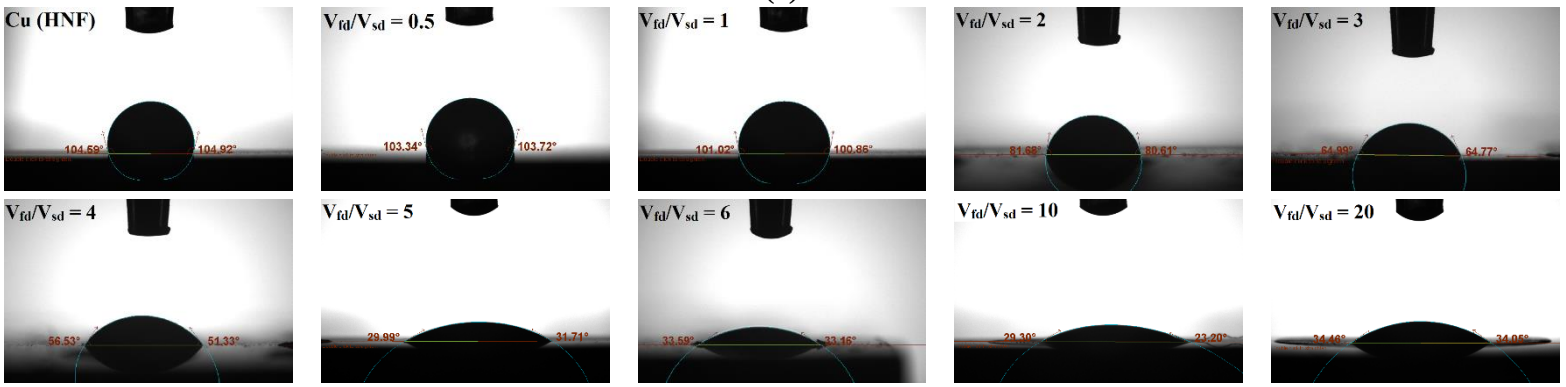


(b)

Fig. 3 (a) Net evaporation rate of water droplet over a copper surface (Cu ($H_2O$)) and the Cu-$Al_2O_3$ HNF droplet over a copper (Cu (HNF)) and its residue surface for various residue sizes ($V_{fd}/V_{sd}$ = 0.5-20), (b) Cu-$Al_2O_3$ HNF droplet images at quasi-equilibrium state resting on copper (Cu (HNF)) and residue surfaces ($V_{fd}/V_{sd}$ = 0.5-20).

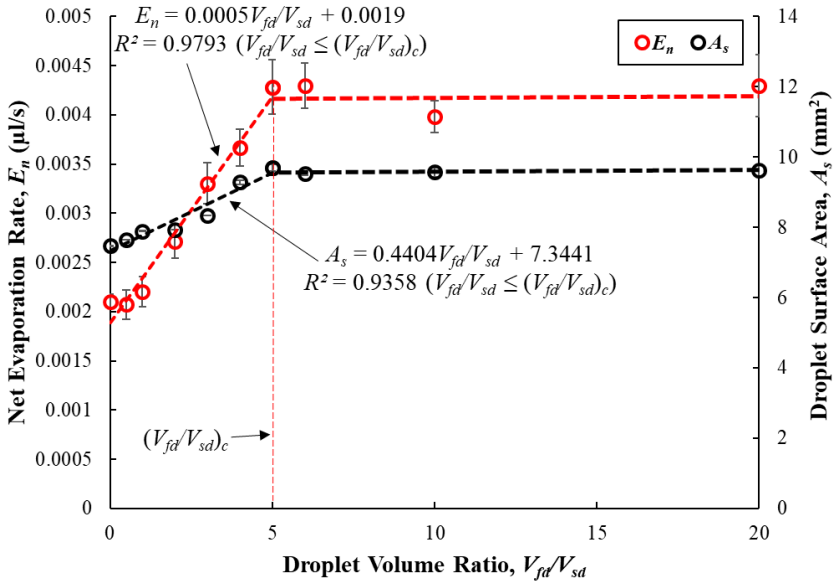


(a)

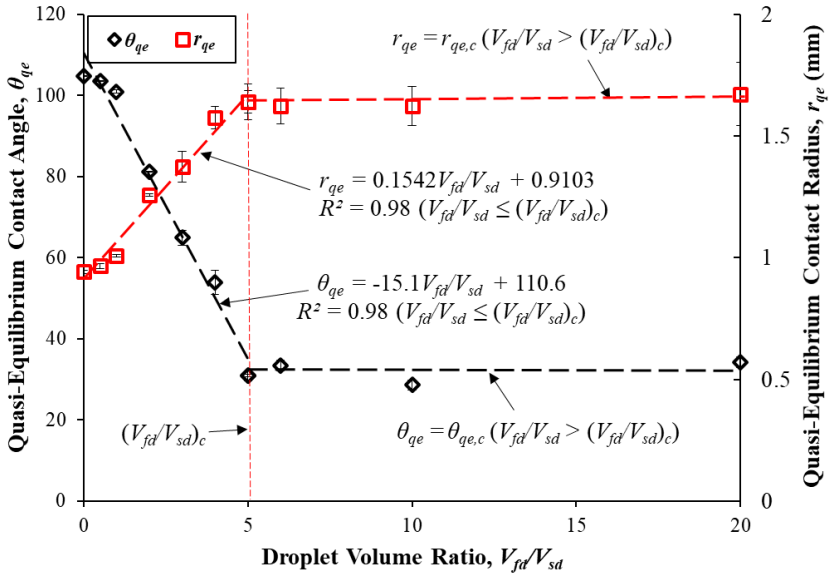


(b)

Fig. 4 (a) Variation of the Cu-$Al_2O_3$ HNF net droplet evaporation rate and quasi-equilibrium droplet surface area (droplet-air interfacial area) with droplet volume ratio, (b) variation of droplet contact angle and contact radius at quasi-equilibrium state with droplet volume ratio. $V_{fd}/V_{sd} = 0$ refers to the Cu-$Al_2O_3$ HNF droplet resting on a copper surface.

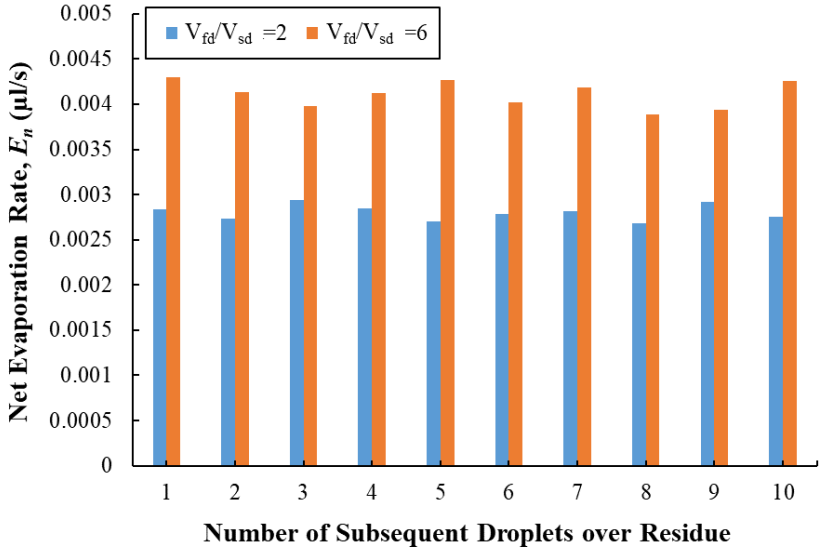


(a)

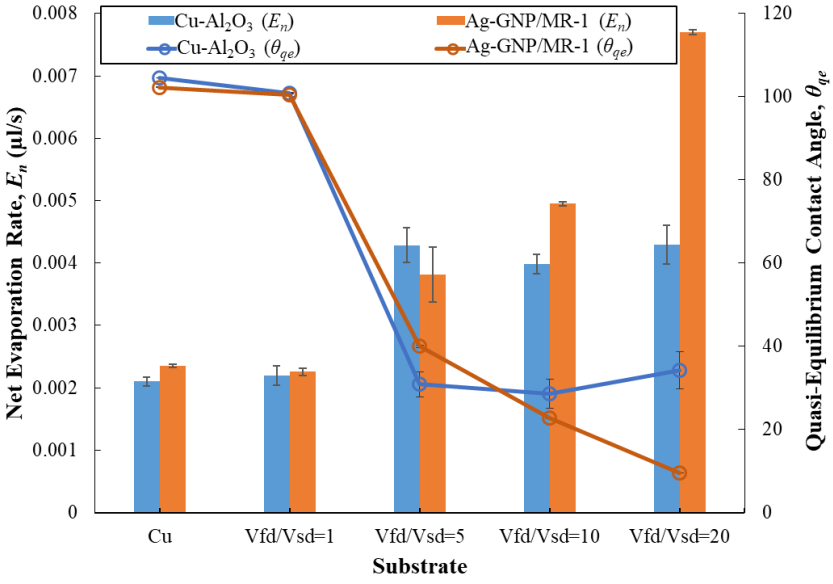


(b)

Fig. 5 (a) Net evaporation rate for subsequent Cu-$Al_2O_3$ hybrid nanofluid droplets over the residue formed by the first evaporated droplet, (b) comparison of net evaporation rate and the quasi-equilibrium contact angle of Cu-$Al_2O_3$ hybrid nanofluid and Ag-GNP/MR-1 hybrid nanofluid [39] droplets over copper and their respective residue surfaces.

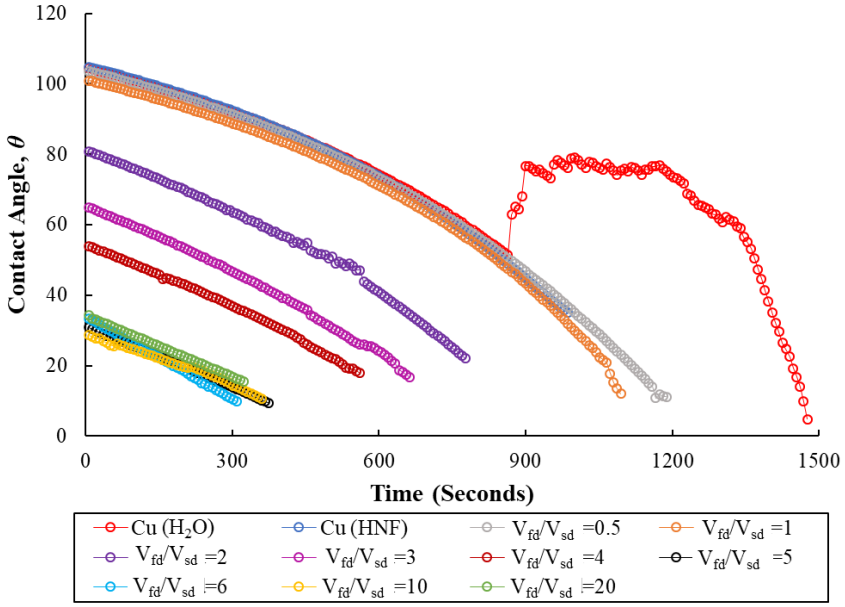


Fig. 6 Contact angle variation of water droplet on a copper surface (Cu ($H_2O$)) and the Cu-$Al_2O_3$ HNF droplet on copper (Cu (HNF)) and residue surfaces ($V_{fd}/V_{sd}$ = 0.5-20) with time.

838

839

840

841

842

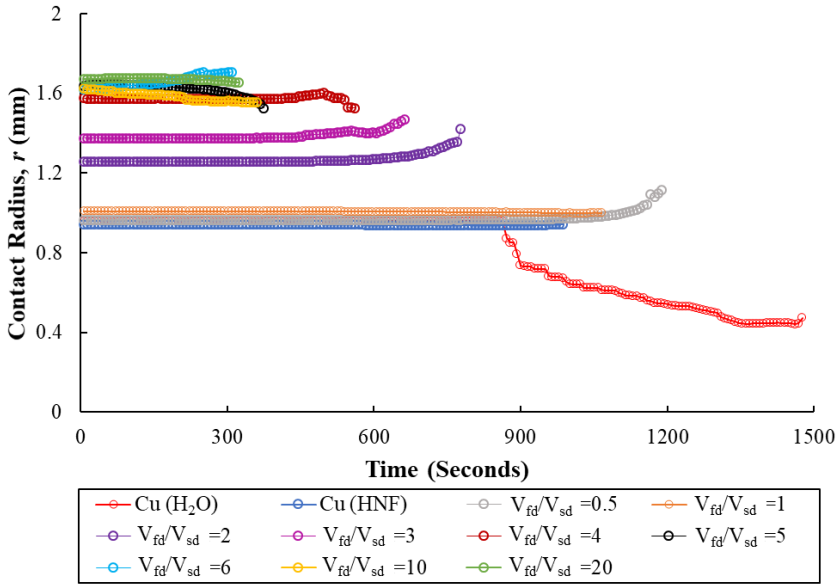


843

844 Fig. 7 Contact radius variation of water droplet on a copper surface (Cu ($H_2O$)) and the Cu-$Al_2O_3$

845 HNF droplet on copper (Cu (HNF)) and residue surfaces ($V_{fd}/V_{sd}$ = 0.5-20) with time.

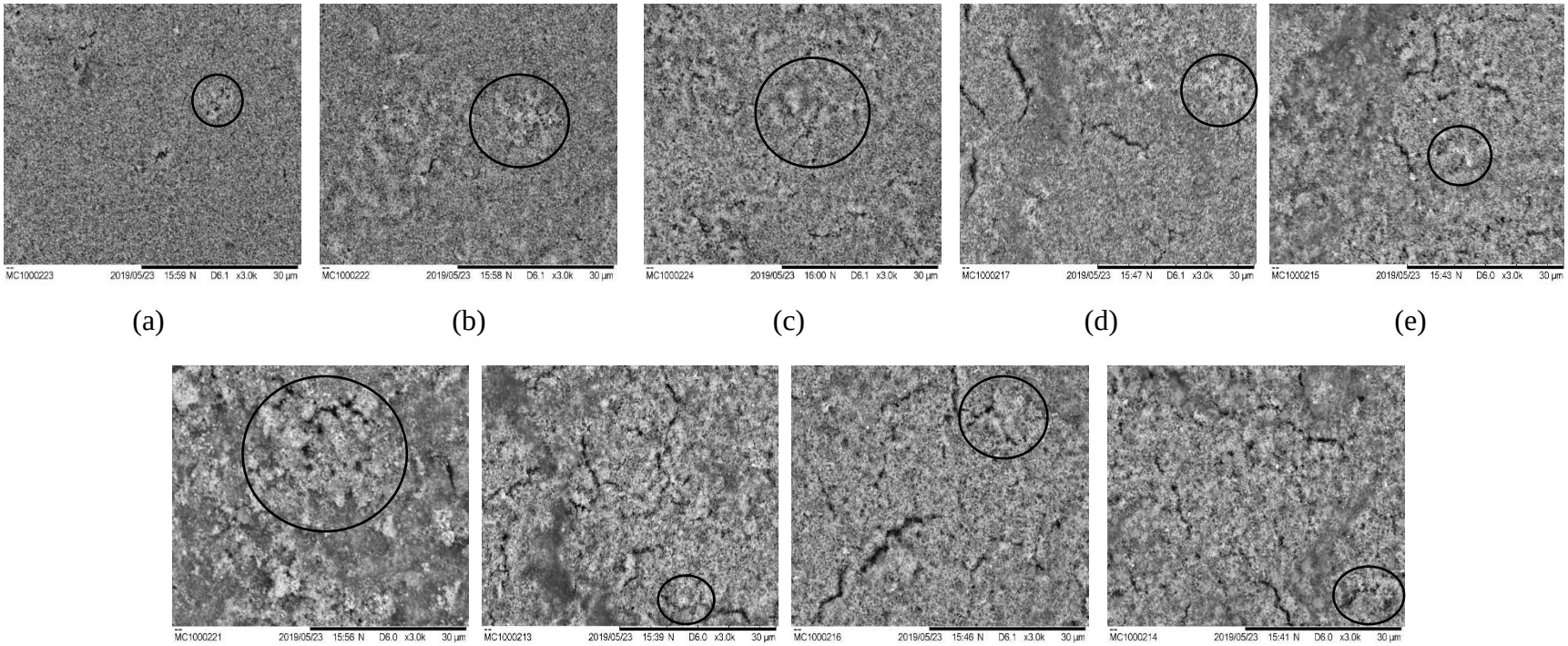


Fig. 8 SEM micrographs of Cu-$Al_2O_3$ HNF droplet residues obtained from droplet volumes ($V_{fd}$) of (a) 1.5 µl, (b) 3 µl, (c) 6 µl, (d) 9 µl, (e) 12 µl, (f) 15 µl, (g) 18 µl, (h) 30 µl and (i) 60 µl. Circles show the presence of clustered hybrid nanoparticles on residue surfaces.

853

854

855

856 Table 1 Copper and the Cu-$Al_2O_3$ HNF droplet residue surface characteristics. Uncertainties for first droplet volume ($V_{fd}$) are obtained
857 from manufacturer [49].

| Substrate | First droplet volume, $V_{fd}$ (µl) | Droplet residue radius, $r_{res}$ (mm) | Residue surface particle density, $\rho_{res}$ (µl/mm$^2$) | Roughness ratio, $a$ | Average surface roughness (µm) | Areal porosity (%) | Mean pore (Feret) diameter (µm) |
|---|---|---|---|---|---|---|---|
| **Copper** | - | - | - | 1.004±0.001 | 0.084±0.002 | - | - |
| **Residue** | 1.5±0.05 | 0.965±0.013 | 0.00051±0.00002 | 1.211±0.013 | 1.377±0.018 | 2.372±0.087 | 0.196±0.004 |
| | 3±0.06 | 1.018±0.035 | 0.00092±0.00005 | 1.292±0.009 | 1.521±0.031 | 2.413±0.040 | 0.207±0.006 |
| | 6±0.15 | 1.258±0.021 | 0.00120±0.00005 | 1.315±0.008 | 1.657±0.022 | 2.682±0.148 | 0.287±0.011 |
| | 9±0.15 | 1.374±0.058 | 0.00152±0.00009 | 1.374±0.005 | 2.683±0.086 | 2.791±0.132 | 0.264±0.013 |
| | 12±0.15 | 1.574±0.063 | 0.00154±0.00008 | 1.396±0.010 | 2.892±0.094 | 2.827±0.093 | 0.295±0.024 |
| | 15±0.25 | 1.642±0.095 | 0.00178±0.00013 | 1.459±0.007 | 3.285±0.049 | 2.956±0.257 | 0.355±0.061 |
| | 18±0.25 | 1.781±0.042 | 0.00181±0.00007 | 1.471±0.003 | 3.414±0.079 | 3.873±0.115 | 0.312±0.032 |
| | 30±0.25 | 2.201±0.040 | 0.00197±0.00005 | 1.641±0.011 | 3.932±0.027 | 2.934±0.276 | 0.247±0.014 |
| | 60±0.50 | 2.984±0.103 | 0.00214±0.00008 | 1.699±0.017 | 4.169±0.038 | 3.222±0.168 | 0.292±0.003 |

858

859

860

Table 2 Surface free energy of substrates and its effect on wetting and evaporation rate of the Cu-$Al_2O_3$ HNF droplet.

| **Substrate** | **Droplet volume ratio, $V_{fd}$ / $V_{sd}$** | **Net surface free energy, $\gamma_{sv}$ (mN/m)** | **Polar surface free energy, $\gamma_{sv}{}^{p}$ (mN/m)** | **Dispersive surface free energy, $\gamma_{sv}{}^{d}$ (mN/m)** | **Quasi-equilibrium contact angle, $\theta_{qe}$** | **Net evaporation rate, $E_n$ (µl/s)** |
|---|---|---|---|---|---|---|
| **Copper** | - | 32.901±0.816 | 0.075±0.352 | 32.825±0.464 | 104.759±0.116 | 0.0021±0.0001 |
| **Residue** | 20 | 41.286±1.979 | 14.149±1.231 | 27.137±0.749 | 34.258±0.145 | 0.0043±0.0003 |